



# 1 Two pathways of how SST anomalies drive the interannual 2 variability of autumnal haze days in the Beijing–Tianjin– 3 Hebei region, China

4  
5 **Jing Wang<sup>1</sup>, Zhiwei Zhu<sup>1\*</sup>, Li Qi<sup>1</sup>, Qiaohua Zhao<sup>1</sup>, Jinhai He<sup>1</sup>, and Julian X. L. Wang<sup>2</sup>**

6 <sup>1</sup>Key Laboratory of Meteorological Disaster, Ministry of Education (KLME)/Joint International Research Laboratory of Climate and  
7 Environment Change (ILCEC)/Collaborative Innovation Center on Forecast and Evaluation of Meteorological Disasters (CIC-FEMD),  
8 Nanjing University of Information Science and Technology, Nanjing, China

9 <sup>2</sup>Air Resources Laboratory, National Oceanic and Atmospheric Administration, College Park, MD, USA

10  
11 \* Correspondence to: Zhiwei Zhu (zww@nuist.edu.cn)

12  
13 **Abstract.** Analogous to the circumstances in wintertime, the increasing severity of autumnal haze pollution over  
14 the Beijing–Tianjin–Hebei (BTH) region may also lead to impairment of the socioeconomic development and  
15 human health in this region. Despite manmade aerosol emissions, the interannual variability of autumnal  
16 (September–October–November) haze days (AHD) in the BTH region ( $AHD_{BTH}$ ) is apparently tied to the global  
17 and regional meteorological anomalies. The present study suggests that an above-normal  $AHD_{BTH}$  is closely  
18 associated with the simultaneous sea surface temperature (SST) warming in two regions [over the North Atlantic  
19 subtropical sector (R1) and over the western North Pacific sector (R2)]. When the autumnal SST warming in R1  
20 and R2 are both remarkably significant, the joint impacts can greatly enhance the likelihood of a higher  $AHD_{BTH}$ .  
21 Observational and simulation evidence suggests that SST anomalies can affect the variation in  $AHD_{BTH}$  via two  
22 different pathways. Firstly, SST warming in R1 can induce a downstream mid-latitude Rossby wave train,  
23 leading to a barotropic high-pressure and subsidence anomaly over the BTH region. Secondly, SST warming in R2  
24 can also result in air subsidence over the BTH region through an anomalous local meridional cell. Through these  
25 two distinct pathways, localized meteorological circumstances conducive to a higher  $AHD_{BTH}$  (i.e., repressed  
26 planetary boundary layer, weak southerly airflow, and warm and moist conditions) can be established.

## 27 28 29 **1 Introduction**

30 Aerosol particles (APs) are ubiquitous in the ambient air. Through aerosol-induced forcing, APs  
31 can exert profound impacts on regional and large-scale circulation (e.g., Chung et al., 2002; Lau  
32 and Kim, 2006; Lau et al., 2006; Liu et al., 2009; Li et al., 2016; Wu et al., 2016), as well as global  
33 warming (e.g., Charlson et al., 1992; Tett et al., 1999; Zhang et al., 2016). Notably, due to the  
34 property of light extinction related to high concentrations of APs, especially fine particulate matter  
35 [i.e., particulate matter (PM) with an aerodynamic diameter of 2.5  $\mu\text{m}$  or less ( $PM_{2.5}$ )] (Guo et al.,  
36 2014; Wang et al., 2014; Li et al., 2017; Seo et al., 2017; Chen et al., 2018; Luan et al., 2018),  
37 severe haze weather with low visibility and high concentrations of gas pollutants can readily occur  
38 (Chen et al., 2012; Li et al., 2016; Ding et al., 2017; Seo et al., 2017; Chen et al., 2018).

39 In recent decades, observational evidence suggests that China has become one of the most severe  
40 AP-loading regions in the world (Tao et al., 2016; Li et al., 2016), arguably because of the  
41 country's rapid industrialization and urbanization (Xu et al., 2015; Zhang et al., 2016). High  
42 concentrations of APs can lead to the formation of severe haze weather via complicated  
43 interactions (Wang et al., 2014). Haze weather is not only harmful to the human respiratory and  
44 cardiovascular systems (Pope III and Dockery, 2006; Tie et al., 2009; Chen et al., 2013; Xu et al.,  
45 2013), but also influences vehicular traffic and crop yields (Chameides et al., 1999; Wu et al.,  
46 2005). As a result, haze pollution has received considerable attention from both the government  
47 and the public. Unfortunately, on the one hand, overwhelming industrialization leads to more  
48 severe haze contamination over the Beijing–Tianjin–Hebei (BTH) region (Yin et al., 2015); whilst



49 on the other hand, the trumpet-shaped topography (Fig. 1) of the region is unfavorable for the  
50 dissipation of air pollution, thus making the BTH region home to some of the worst haze weather  
51 in China. Since the BTH region is the most economically developed region in North China and is  
52 at the heart of Chinese politics and culture (not least because it is home to the capital city, Beijing,  
53 and Xiongan New Area, for instance), severe haze pollution in this region has become a critical  
54 issue (e.g., Mu and Zhang, 2014; Yin et al., 2015; Wang, 2018), especially since the unprecedented  
55 severe haze event in North China in January 2013 (Wang et al., 2014; Zhang et al., 2014; Mu and  
56 Zhang, 2014; Tao et al., 2014; Zhang et al., 2015).

57 To date, numerous efforts have been made to explore the causes of wintertime haze pollution over  
58 the BTH region and its surroundings, and these efforts roughly fall into three categories of results  
59 from the climatological perspective. The first category features studies that have reported that the  
60 joint effects of the emissions of various sources of APs (e.g., Cao et al., 2007; Guo et al., 2011;  
61 Zhu et al., 2016) and climate anomalies (e.g., Chen and Wang, 2015; Wang and Chen, 2016; Yin  
62 and Wang, 2016a; Cai et al., 2017; Yin et al., 2017; Yin and Wang, 2018; Wang, 2018) may have  
63 brought about the increasing severity of haze pollution over China in recent decades. The second  
64 category of studies, meanwhile, underlines the causality of the variation in winter haze days in  
65 eastern and northern China from the perspective of climate anomalies (e.g., Li et al., 2016; Yin  
66 and Wang, 2016b; Yin and Wang, 2018; Pei et al., 2018). For instance, a weakened East Asian  
67 winter monsoon (EAWM) system has been suggested as being responsible for above-normal  
68 numbers of winter haze days (e.g., Niu et al., 2010; Li et al., 2016; Yin and Wang, 2016a; Yin and  
69 Wang, 2017; Yin et al., 2017); plus, the EAWM's variability has been shown to be significantly  
70 tied to the East Atlantic–West Russia pattern (Yin et al., 2017; Yin and Wang, 2017) and Eurasian  
71 pattern (Zhang et al., 2016; Yin et al., 2017). The third category of studies focuses on the external  
72 forcings associated with the variability of winter haze days. These forcings include the sea surface  
73 temperature (SST) (e.g., Gao and Li, 2015; Wang et al., 2015; Yin and Wang, 2016a; Yin et al.,  
74 2017), Arctic sea ice (e.g., Wang et al., 2015; Zou et al., 2017), Eurasian snowpack (e.g., Yin and  
75 Wang, 2017; Yin and Wang, 2018), and the thermal conditions on the Tibetan Plateau (e.g., Xu et  
76 al., 2016). However, most of these previous works have focused on wintertime, with little  
77 attention having been paid to other seasons.

78 Autumn is a transitional season from the wet and hot conditions of summer to the dry and cold  
79 conditions of winter. The weather in autumn over the BTH region is climatologically quite  
80 pleasant, with favorable temperatures and light winds. Outdoor activities and tourism are therefore  
81 important, economically, in the autumn season. However, notably, autumn is also a season in  
82 which haze weather frequently occurs in the BTH region (Chen and Wang, 2015), and the number  
83 of autumnal haze days (AHDs) has increased remarkably in recent years. Such an increase in the  
84 number of haze days is a potential threat to the outdoor activities and tourism that, as mentioned,  
85 are so important to the region at this time of year. Therefore, research into the causes of the  
86 interannual variation in AHDs in the BTH region ( $AHD_{BTH}$ ) is imperative. Such work not only  
87 provides scientific support to the year-to-year scheduling of anthropogenic emissions for dealing  
88 with autumnal haze pollution, but also helps the government with facilitating the arrangement of  
89 tourism and outdoor activities. However, as already mentioned, compared to the myriad  
90 publications on wintertime haze pollution, autumn haze pollution over the BTH region has  
91 attracted far less attention, with only a few case studies on atmospheric circulation having been  
92 reported (Yang et al., 2015; Gao and Chen, 2017; Wang et al., 2018). It was this knowledge gap  
93 that motivated us to revisit the variability of  $AHD_{BTH}$ . Considering that the SST acts as a crucial  
94 driver of large-scale climate variability (e.g., Wang et al., 2009; Zhu et al., 2014; He and Zhu,  
95 2015; Xiao et al., 2015; Zhu and Li, 2017; Zhu, 2018), we aimed to figure out the underlying air–  
96 sea interaction mechanisms for the interannual  $AHD_{BTH}$  variability in the present study.



97 The remainder of this paper is organized as follows. Section 2 introduces the data, model and  
98 methodology. Section 3 presents the atmospheric anomalies associated with  $AHD_{BTH}$ . Section 4  
99 addresses the mechanisms and pathways of SST anomalies (SSTAs) in driving the interannual  
100 variations of  $AHD_{BTH}$ . Conclusions and further discussion are provided in the final section.

101

## 102 **2 Data, model and methodology**

103

### 104 **2.1 Data**

105 The data used in this study are as follows: (1) monthly mean planetary boundary layer height  
106 (PBLH), with a  $1^\circ \times 1^\circ$  horizontal resolution, from the European Centre for Medium-Range  
107 Weather Forecasts Interim Reanalysis (ERA-Interim) (Dee et al., 2011); (2) monthly mean  
108 atmospheric data, with a  $2.5^\circ \times 2.5^\circ$  horizontal resolution, from the National Centers for  
109 Environmental Prediction (NCEP)–National Center for Atmospheric Research (NCAR)  
110 Reanalysis I (NCEP/NCAR) (Kalnay et al., 1996); and total cloud cover (entire atmosphere  
111 considered as a single layer;  $192 \times 94$  points in the horizontal direction), also from NCEP/NCAR;  
112 (3) monthly mean SST, with a  $2^\circ \times 2^\circ$  horizontal resolution, of the Extended Reconstructed SST  
113 dataset, version 5 (ERSST.v5; Huang et al., 2017), from the National Oceanic and Atmospheric  
114 Administration (NOAA); (4) global monthly precipitation data, with a  $2.5^\circ \times 2.5^\circ$  horizontal  
115 resolution, from NOAA's precipitation reconstruction (Chen et al., 2002); (5) ground-timing  
116 observation datasets, at 02:00, 08:00, 14:00 and 20:00 BLT (Beijing local time), from the National  
117 Meteorological Information Center of China. The temporal coverage of the PBLH data is from  
118 1979 to 2017, while the remaining datasets are from 1960 to 2017. Here, boreal autumn refers to  
119 the seasonal mean for September–October–November (SON).

120

### 121 **2.2 Model**

122 The numerical model used here is an anomaly atmospheric general circulation model (AGCM)  
123 based on the Geophysical Fluid Dynamics Laboratory (GFDL) global spectrum dry AGCM (Held  
124 and Suarez, 1994), which is employed to investigate the mechanisms for the atmospheric  
125 responses to the specified SST-induced heating. The horizontal resolution is T42, with five evenly  
126 spaced sigma levels ( $\sigma = p/ps$ ; interval: 0.2; top level:  $\sigma = 0$ ; bottom level:  $\sigma = 1$ ). A realistic  
127 autumn mean state, obtained from the long-term mean of the NCEP/NCAR reanalysis data, is  
128 prescribed as the model basic state. This model has been used to unravel the eddy–mean  
129 interaction over East Asia and its downstream impacts on North American climate (Zhu and Li,  
130 2016, 2018).

131

### 132 **2.3 Methodology**

133 The definition of a haze day in the present study is identical to that used in previous studies (Chen  
134 and Wang, 2015; Yin et al., 2017; Pei et al., 2018). It is based on the ground-timing observations  
135 of relative humidity, visibility and wind speed. It is important to point out that the visibility  
136 observations switched from manual to automatic in 2014, and the visibility threshold for haze was  
137 thus also slightly modified from then on. However, the continuity of the data was not affected.  
138 Following Zhang et al. (2016), the mean number of haze days ( $\overline{NHD}$ ) for  $AHD_{BTH}$  was computed  
139 by:



$$\overline{\text{NHD}} = \frac{1}{n} \sum_{i=1}^n N \quad (1)$$

141 where  $n$  (here,  $n = 20$ ) is the number of meteorological sites distributed within the BTH region  
142 (Fig. 1), and  $N$  denotes the number of haze days at a site for each autumn.

143 Similar to the approach proposed by Zhu and Li (2017), the 9-yr running mean of the  $\text{AHD}_{\text{BTH}}$   
144 was used to represent the interdecadal component of the  $\text{AHD}_{\text{BTH}}$ , whereas the interannual  
145 component was obtained by removing the interdecadal component from the raw  $\text{AHD}_{\text{BTH}}$ . Since  
146 there is a tapering problem when calculating the running mean, the first four years and the last  
147 four years of the interdecadal component of the  $\text{AHD}_{\text{BTH}}$  could be estimated by the mean value of  
148 the available data with a shorter window. For example, the interdecadal component of the  $\text{AHD}_{\text{BTH}}$   
149 for 2016 and 2017 could be obtained by the mean of 2012–17 and 2013–17, respectively. Note  
150 that the temporal correlation coefficients (TCCs) between the  $\text{AHD}_{\text{BTH}}$  and every single site were  
151 all positive and significant (Fig. 1), indicating coherency in the interannual variability of haze days  
152 over the BTH region; plus, the distribution of these sites was also fairly even. Therefore, the  
153 interannual component of the  $\text{AHD}_{\text{BTH}}$  could be used as a good representation of the year-to-year  
154 pollution state over the whole BTH region in autumn.

155 Linear regression, composite analysis and correlation were used to examine the associated  
156 circulation and SSTAs. The two-tailed Student's  $t$ -test was employed to evaluate the statistical  
157 significance of these analyses. The wave activity flux (WAF; Takaya and Nakamura, 2001) was  
158 calculated to depict the tendency of Rossby wave energy propagation.

159

### 160 3 Atmospheric anomalies associated with the interannual changes of $\text{AHD}_{\text{BTH}}$

161 Figure 2 illustrates the time series of the raw  $\text{AHD}_{\text{BTH}}$ , along with its interdecadal and interannual  
162 components. A prominent feature is that the  $\text{AHD}_{\text{BTH}}$  displays both interannual and interdecadal  
163 variability. On the interdecadal timescale, the  $\text{AHD}_{\text{BTH}}$  was below average during 1960–1975 and  
164 the late-2000s, but above average during 1975–2003, and it increased dramatically after 2009. On  
165 the interannual timescale, the  $\text{AHD}_{\text{BTH}}$  presents large differences year on year. For example, the  
166  $\text{AHD}_{\text{BTH}}$  was at its lowest in 2012, but peaked in 2014. Since the interannual variability explains  
167 most of the variances in the  $\text{AHD}_{\text{BTH}}$  variability, in this study we only investigate the atmospheric  
168 anomalies and unravel the underlying physical mechanisms and pathways associated with the  
169  $\text{AHD}_{\text{BTH}}$  on the interannual timescale.

170 Close scrutiny of the large-scale and localized dynamic and thermodynamic fields associated with  
171 the  $\text{AHD}_{\text{BTH}}$  should help in advancing our understanding of the possible underlying mechanisms.  
172 In this regard, we firstly examine the climatological mean autumnal 500-hPa geopotential height  
173 ( $Z_{500}$ ), 850-hPa winds (UV850) and total cloud, along with the surface relative humidity and  
174 surface air temperature that potentially impact the climate over the BTH region (Fig. 3). There is a  
175 shallow mid-tropospheric trough over coastal East Asia (Fig. 3a), which resembles the trough in  
176 winter (Zhao et al., 2018; Pei et al., 2018) but with a smaller magnitude. Behind the trough, a clear  
177 anticyclonic circulation appears over the central-eastern China, with remarkable  
178 westerly/northwesterly winds dominating the BTH region (Fig. 3a). Cold and dry air from higher  
179 latitudes is advected by the winds, and the BTH region is thus much cooler and drier and has less  
180 cloud than other regions at the same latitudes (e.g., the central portion of Japan). As such, the  
181 autumnal BTH region features breezy and windy conditions climatologically, with low surface  
182 relative humidity (Fig. 3b), reducing the likelihood of haze there via the effect of cold  
183 advection/ventilation. Note, however, that if the breezy conditions are interrupted, haze pollution



184 may be enhanced. One may ask whether a higher  $AHD_{BTH}$  is related to the interference of such  
185 breezy conditions. Figures 4 and 5 were therefore plotted to examine the associated atmospheric  
186 parameters/circulations. For simplicity, the regression and composite analyses in this study  
187 reported hereafter are interpreted with respect to positive phase of  $AHD_{BTH}$  anomalies only.

188 Previous studies have revealed that haze pollution is closely correlated with local meteorological  
189 parameters in the planetary boundary layer (e.g., You et al., 2017; Chen et al., 2018). Figure 4  
190 suggests that an above-normal  $AHD_{BTH}$  is tied to a localized enhancement of surface relative  
191 humidity (Fig. 4a) and temperature (Fig. 4b), along with suppressed surface wind speed (Fig. 4c),  
192 sea-level pressure (SLP) (Fig. 4d) and PBLH (Fig. 4e). Specifically, it seems that autumnal haze  
193 pollution is more significantly correlated with temperature and PBLH. So, what causes the above  
194 anomalous parameters that are favorable for a higher  $AHD_{BTH}$ ?

195 Figure 5 shows the associated large-scale atmospheric circulation anomalies at different levels of  
196 troposphere. From Figs. 5a–5d, the most noticeable feature is that there is a planetary-scale,  
197 quasi-barotropic Rossby wave train emanating from the North Atlantic subtropical sector. In  
198 addition to an anticyclonic anomaly centered over the North Atlantic subtropics, this  
199 teleconnection pattern has another two pairs of anomalous cyclones (low pressure) and  
200 anticyclones (high pressure) stretching across Eurasia to the North Pacific, i.e., a cyclonic  
201 anomaly centered over the ocean south of Greenland, an anticyclonic anomaly centered over  
202 Scandinavia, a cyclonic anomaly centered over the adjacent central Siberia, and a Northeast Asian  
203 anticyclonic anomaly centered over the Sea of Japan (SJ). In general, based on the regressed  
204 atmospheric fields, the teleconnection has a much larger amplitude in the upper troposphere (Fig.  
205 5a), rather than in the mid-troposphere (Fig. 5b) and lower troposphere (Fig. 5c).

206 Among all the height anomalies within the teleconnection, the anomalous quasi-barotropic  
207 Northeast Asian anticyclonic anomaly centered over the SJ ( $A_{SJ}$ ) plays a direct role in driving a  
208 higher  $AHD_{BTH}$ . The related physico-meteorological causes are as follows: There are  
209 southerly/southeasterly anomalies along the western flank of the  $A_{SJ}$  in the lower troposphere (Figs.  
210 5c and 5d), manifesting the capability of suppressed atmospheric horizontal diffusion and thus  
211 favoring a buildup of substantial local and nonlocal APs and warmer moisture over the BTH  
212 region (Yang et al., 2015; Yang et al., 2016) under the specific topographical forcing of the  
213 Taihang Mountains and Yan Mountains (Fig. 1). On the other hand, the significant positive  
214 pressure anomaly in the mid-to-upper parts of the  $A_{SJ}$  (Figs. 5a and 5b) not only impedes the  
215 intrusion of cold air into the BTH region, but also facilitates consistent air subsidence over the  
216 BTH region and its surrounding areas (Fig. 4f), resulting in the decrease of the PBLH and  
217 amplification of static stability (i.e., the dampened vertical dispersion of the atmosphere).  
218 Consequently, the meteorological conditions connected to a higher  $AHD_{BTH}$  are quite different  
219 from the climatological characteristics (Fig. 3).

220 To summarize, the  $A_{SJ}$  and the associated subsidence can induce the capacity for suppressed local  
221 horizontal and vertical dispersion over the BTH region and its surrounding areas, as shown in the  
222 above-mentioned anomalous parameters in the boundary layer (Fig. 4); and these parameters are  
223 further responsible for the accumulation and secondary formation/hygroscopic growth of APs  
224 (Jacob and Winner, 2009; Ding and Liu, 2014; Mu and Liao, 2014; Jia et al., 2015). As such, the  
225 haze pollution over the BTH region is readily established within a narrow space. The question of  
226 how the above-normal  $AHD_{BTH}$  is stimulated could plausibly be transferred into questioning the  
227 pathways of how the  $A_{SJ}$  is developed and sustained. In fact, the  $A_{SJ}$  and the associated air  
228 subsidence are modulated by SSTAs. We tackle this issue in the next section.

229



## 230 4 Possible mechanisms and pathways

231

### 232 4.1 Observational diagnoses

233 Figure 5c shows that an above-normal  $AHD_{BTH}$  is closely correlated with SST warming in two key  
234 regions: the North Atlantic subtropical sector (R1: 22°–32°N, 90°–40°W), and the western North  
235 Pacific sector (R2: 10°–30°N, 108°–140°E). Meanwhile, from Fig. 5e we can discern that  
236 enhanced and significant precipitation appears to the north of R1, indicating an active atmospheric  
237 response to the SST warming over R1; whereas, there is an insignificant positive precipitation  
238 signal over R2 and its surrounding areas. Figure 6 further depicts that the SON SSTs over both R1  
239 and R2 are positively correlated with  $AHD_{BTH}$ , and the TCC between the  $AHD_{BTH}$  and SON SST  
240 over R1 (R2) is 0.45 (0.28), exceeding the 99% (95%) confidence level. By virtue of the above  
241 analyses, we speculate that the SST over R1 may play a more important role than that over R2 in  
242 driving a higher  $AHD_{BTH}$ . Note, however, that when the SON SSTs over R1 and R2 are both  
243 obviously elevated, the  $AHD_{BTH}$  is more likely to be higher than normal, such as in 1980, 1987  
244 and 2015. Furthermore, as indicated above, the  $AHD_{BTH}$  is closely correlated with the  $A_{SJ}$  and the  
245 associated air subsidence, which allows us to speculate that the positive SSTAs over R1 and R2  
246 might drive the interannual variability of  $AHD_{BTH}$  by modulating the intensity of the  $A_{SJ}$  and  
247 associated subsidence. To validate this hypothesis, we firstly examine pathway of SSTAs over R1  
248 in driving  $AHD_{BTH}$ .

249 Figure 5c suggests that the SST warming in R1 may induce larger-area concomitant low-level  
250 easterly anomalies, which mainly form over the southeastern portion of R1 and the area to its  
251 south. In such a scenario, an anticyclonic anomaly is induced (Fig. 5c), with its center to the  
252 northeast of R1. Along the western flank of this anticyclonic anomaly, warm and moist airflows  
253 move northwards. When these warm and moist airflows meet cold air mass in the areas to the  
254 north of R1, enhanced precipitation is thus generated (Fig. 5e). Meanwhile, the resultant enhanced  
255 rainfall condensation heating induces a cyclonic anomaly to its north, thereby exciting the other  
256 two pairs of the aforementioned teleconnection pattern along the westerly jet, as demonstrated by  
257 the Rossby wave train induced by SST warming in R1 (Figs. 7 and 8). Specifically, from the  
258 regressed SON UV850 (Fig. 7), we can see that the SST warming in R1 can indeed induce a  
259 significant low-level teleconnection pattern arising from the North Atlantic subtropics, bearing a  
260 close resemblance to that in Fig. 5c; and to the north of R1, where the rainfall condensation  
261 heating is triggered, the corresponding WAF exhibits a distinctive arc-shaped trajectory, perturbing  
262 the other two pairs of cyclones and anticyclones of the teleconnection (Fig. 8). This teleconnection  
263 extends from the North Atlantic towards Scandinavia, goes through the Eurasia and arrives at the  
264 western North Pacific. Therefore, by means of this trajectory, Rossby wave energy in the middle  
265 (Fig. 8b) and upper (Fig. 8a) troposphere may propagate southeastwards into the  $A_{SJ}$  and its  
266 surrounding region, favoring the formation/sustainability of the  $A_{SJ}$  and the associated air  
267 subsidence. In this context, the associated meteorological parameters (Fig. S1), which resemble  
268 those tied to a higher  $AHD_{BTH}$  (Fig. 4), might increase the likelihood of SON haze pollution over  
269 the BTH region. Again, this induced teleconnection is quasi-barotropic in structure, with its  
270 magnitude larger in the upper troposphere (Fig. 8a), which is consistent with that in Fig. 5a.

271 When focusing on region R2 (Fig. 9a), we find that, corresponding to the SSTAs over R2, there  
272 exists a cyclonic anomaly to the west of R2. Besides, substantial SSTA-induced low-level easterly  
273 anomalies are mainly located to the southeast of R2; plus, a huge anticyclonic anomaly to the  
274 northeast is excited, with its center situated over the northern Pacific. In such a scenario, R2 is  
275 thoroughly penetrated by significant warm and humid airflows transported from the eastern flank



276 of the cyclonic and the western flank of anticyclonic anomaly respectively (Fig. 9a), warming the  
277 SST over R2. Furthermore, the airflow convergence primarily occurs over the southwestern  
278 portion of R2, where the strongly significant and positive rainfall anomaly is triggered (Fig. 9b).  
279 Thus, the enhanced significant rainfall heating perturbation may greatly intensify the ascending  
280 motion over R2 and the adjacent region, resulting in subsidence over the BTH region and  
281 Northeast Asia via an anomalous local meridional cell (Fig. 10a). As such, the BTH region and its  
282 adjacent areas are dominated by significant warm temperatures in the middle and upper  
283 troposphere (Fig. 10b), leading to the maintenance and reinforcement of the  $A_{SJ}$  and the downward  
284 motions over the BTH region, as well as the regional low-level stability. Under such  
285 circumstances, the vertical transport of APs is restricted (Zhang et al., 2014; Pei et al., 2018), and  
286 the near-surface winds are weakened (Li et al., 2016). Meanwhile, the parameters associated with  
287 SST warming in R2 (Fig. S2) also support the formation of haze weather over the BTH region.

288

#### 289 4.2 Numerical model simulations

290 Two experiments were conducted to further validate the above-mentioned two pathways in how  
291 SSTAs drive the variation of  $AHD_{BTH}$ . The first experiment (H\_NAS) simulated the responses to  
292 the heating induced by SSTAs over R1 (Fig. 11). H\_NAS was imposed with a specified heating  
293 centered over the region to the north of R1 (center: 37.67°N, 64.69°W) that largely matched with  
294 the SON positive rainfall anomaly as shown in Fig. 5e. The second experiment (H\_WNP)  
295 mimicked the responses to the prescribed heating over the neighboring areas of R2 (center:  
296 15.35°N, 109.69°E; Fig. 12), where the corresponding regressed precipitation rate was the most  
297 significant and amplified, as exhibited in Fig. 9b. The heating had a cosine-squared profile in an  
298 elliptical region in the horizontal direction. The maximum heating, with 1 K day<sup>-1</sup> amplitude, was  
299 set to be at 300 hPa.

300 Figure 11 presents the 200- and 500-hPa geopotential height and wind responses to the specified  
301 heating over the North Atlantic subtropical region. As anticipated, the equilibrium state (mean  
302 output from day 40 to day 60) of the Z200 (Fig. 11a) and Z500 (Fig. 11b) responses to the heating  
303 resembles the aforementioned teleconnection (Figs. 5a and 5b), and the simulated response of the  
304 Z200 anomalies is generally larger than its counterpart at 500 hPa (Fig. 11b), which concurs with  
305 the observational evidence. Besides, a similar low-level portion of the  $A_{SJ}$  could also be simulated  
306 (figure not shown). As a result, a strengthened  $A_{SJ}$  is induced.

307 Figure 12 delineates the 850-hPa geopotential height (Z850) and UV850 responses to the specified  
308 heating centered at (15.35°N, 109.69°E). Although there are some differences in spatial  
309 distribution compared with the observations, the well-organized cyclonic anomaly to the west of  
310 the heating center and the anticyclonic anomaly to the north can be properly simulated (Fig. 12).  
311 Meanwhile, the  $A_{SJ}$  and the coherent tropospheric subsidence over the BTH region and the  
312 Northeast Asian anticyclonic anomaly were also simulated well (figure omitted), leading to the  
313 amplified  $A_{SJ}$  as well.

314 To sum up, from observational diagnoses and numerical simulations, we can conclude that there  
315 are two pathways regarding how SSTAs impact the formation and maintenance of the  $A_{SJ}$  and the  
316 associated air subsidence. One pathway operates via a heating-induced large-scale teleconnection  
317 pattern arising from SST warming in R1, and the other is connected to an anomalous local  
318 meridional cell triggered by heating-reinforced ascending motion via local SST warming over R2.

319

320



## 321 5 Conclusions and discussion

322 Motivated by a lack of in-depth understanding with respect to the interannual variations of the  
323  $AHD_{BTH}$ , in the present study we explored the related climate anomalies (localized meteorological  
324 parameters, and large-scale atmospheric and oceanic anomalies) tied to the  $AHD_{BTH}$ . We have  
325 substantiated that an above-normal  $AHD_{BTH}$  is closely correlated with the simultaneous SST  
326 warming in two key regions (R1 over the North Atlantic subtropical sector, and R2 over the  
327 western North Pacific sector), and once the SON SST warming in R1 and R2 are both remarkably  
328 significant, their joint climate impacts can greatly enhance the likelihood of an above-normal  
329  $AHD_{BTH}$ .

330 Potential mechanisms associated with an above-normal  $AHD_{BTH}$  have been proposed through  
331 further investigations. Since the  $A_{SJ}$  and the associated subsidence over the  $A_{SJ}$  and the  
332 surrounding region can yield meteorological circumstances conducive to enhancing the likelihood  
333 of haze pollution in the BTH region, the issue of an above-normal  $AHD_{BTH}$  can be reasonably  
334 transferred into uncovering how the SON  $A_{SJ}$  and associated air subsidence are developed and  
335 sustained. We found that there are two possible pathways. First, SST warming in R1 can induce a  
336 downstream Rossby wave teleconnection, and the associated Rossby wave energy can propagate  
337 into the  $A_{SJ}$  and its surrounding region through an arc-shaped trajectory, developing and  
338 strengthening the  $A_{SJ}$  and the associated subsidence. The other pathway, however, operates  
339 through localized heating-reinforced ascending motion over R2, also resulting in subsidence over  
340 the BTH region and Northeast Asia via an anomalous local meridional cell.

341 AGCM simulations reinforced our hypothesis. With prescribed heating over the region to the north  
342 of R1, a quite similar teleconnection—starting from the North Atlantic subtropics—was excited. If  
343 we imposed an idealized heating over the adjacent R2, where the corresponding precipitation rate  
344 was the most significant and amplified, the concomitant significant low-level convergence around  
345 the heated areas was simulated, enhancing the SST warming in R2 and inducing the  $A_{SJ}$ -resembled  
346 circulation to the north and the subsidence over the BTH region and Northeast Asia. However,  
347 because the model we used is an intermediate anomaly AGCM, and the heating prescribed in the  
348 model is idealized, the simulated patterns were slightly spatially different to those observed.  
349 Although the model cannot reproduce the geopotential height and wind anomalies perfectly, it can  
350 nonetheless support the proposed mechanisms. As a summary, a schematic illustration (Fig. 13) of  
351 the occurrence of a higher  $AHD_{BTH}$  is provided, which encapsulates the major characteristics of  
352 the two pathways of how SSTAs over R1 and R2 drive the  $AHD_{BTH}$  respectively.

353 From the perspective of seasonal prediction, among all the previous individual months of boreal  
354 summer (June–July–August), the SON SST in R1 (R2) was most significantly correlated with the  
355 August SST in R1 (R2) on the interannual timescale, with a TCC of 0.35 (0.61) that exceeded the  
356 95% (99%) confidence level. This suggests that, when the August SST over R1 (R2) is higher, the  
357 subsequent SON SST over R1 (R2) is more likely to become warmer. As such, the previous  
358 August SSTA over R1 (R2) could serve as a possible precursor for the seasonal prediction of the  
359  $AHD_{BTH}$ .

360 In this study, we solely emphasize the potential impacts of SSTAs on the interannual variations of  
361 the  $AHD_{BTH}$ . It should be noted that other external forcings, such as the Arctic sea ice (e.g., Wang  
362 et al., 2015), Eurasian snowpack (e.g., Yin and Wang, 2018), thermal conditions on the Tibetan  
363 Plateau (e.g., Xu et al., 2016) and soil moisture (e.g., Yin and Wang, 2016b), may also exert  
364 profound impacts on haze pollution over China. Studying the mechanisms tied to these forcings  
365 may enhance the seasonal predicting skill for the  $AHD_{BTH}$ . This is an important topic deserving of



366 further exploration.

367

368

369 *Data availability.* The atmospheric data and land-surface data are available from the NCEP/NCAR data archive:  
370 <http://www.esrl.noaa.gov/psd/data/gridded/data.ncep.reanalysis.html> (NCEP/NCAR, 2018). The SST data were downloaded from  
371 <https://www.esrl.noaa.gov/psd/data/gridded/data.noaa.ersst.v5.html> (NOAA, 2018). The precipitation data were downloaded from  
372 <https://www.esrl.noaa.gov/psd/data/gridded/data.prec.html> (NOAA, 2018). The monthly PBLH data are available on the ERA-Interim  
373 website: <http://www.ecmwf.int/en/research/climate-reanalysis/era-interim> (ERA-Interim, 2018). The ground observations are from the  
374 National Meteorological Information Center of China (<http://data.cma.cn/>) (CMA, 2018).

375 *Competing interests.* The authors declare that they have no conflict of interest.

376 *Acknowledgements.* This work was supported by the National Natural Science Foundation of China (Grants 41605035, 41371222, and  
377 41475086) and the Priority Academic Program Development (PAPD) of Jiangsu Higher Education Institutions. Zhiwei was supported by  
378 the Natural Science Foundation of Jiangsu Province (No. BK20161604) and the Startup Foundation for Introducing Talent of NUIST (No.  
379 2018r026).

380

381

382

383

384

385

386

387

388

389

390

391

392

393

394

395

396

397

398

399

400

401

402

403

404

405

406

407

408

409 **References**

- 410 Cai, W. J., Li, K., Liao, H., Wang, H. J., and Wu, L. X.: Weather conditions conducive to Beijing severe haze more  
411 frequent under climate change, *Nat Clim Change*, 7, 257-262, 10.1038/nclimate3249, 2017.
- 412 Cao, J. J., Lee, S. C., Chow, J. C., Watson, J. G., Ho, K. F., Zhang, R. J., Jin, Z. D., Shen, Z. X., Chen, G. C., Kang,  
413 Y. M., Zou, S. C., Zhang, L. Z., Qi, S. H., Dai, M. H., Cheng, Y., and Hu, K.: Spatial and seasonal distributions  
414 of carbonaceous aerosols over China, *J Geophys Res Atmos*, 112, D22S11, 10.1029/2006JD008205, 2007.
- 415 Chameides, W. L., Yu, H., Liu, S. C., Bergin, M., Zhou, X., Mearns, L., Wang, G., Kiang, C. S., Saylor, R. D., Luo,  
416 C., Huang, Y., Steiner, A., and Giorgi, F.: Case study of the effects of atmospheric aerosols and regional haze on  
417 agriculture: An opportunity to enhance crop yields in China through emission controls?, *Proceedings of the*  
418 *National Academy of Sciences*, 96, 13626, 1999.
- 419 Charlson, R. J., Schwartz, S. E., Hales, J. M., Cess, R. D., Coakley Jr, J. A., Hansen, J. E., and Hofmann, D. J.:  
420 Climate forcing by anthropogenic aerosols, *Science*, 255, 423-430, 10.1126/science.255.5043.423, 1992.
- 421 Chen, H. P., and Wang, H. J.: Haze Days in North China and the associated atmospheric circulations based on daily  
422 visibility data from 1960 to 2012, *J Geophys Res Atmos*, 120, 5895-5909, 10.1002/2015JD023225, 2015.
- 423 Chen, J., Zhao, C. S., Ma, N., Liu, P. F., Göbel, T., Hallbauer, E., Deng, Z. Z., Ran, L., Xu, W. Y., Liang, Z., Liu, H.,  
424 J., Yan, P., Zhou, X. J., and Wiedensohler, A.: A parameterization of low visibilities for hazy days in the North  
425 China Plain, *Atmos Chem Phys*, 12, 4935-4950, 10.5194/acp-12-4935-2012, 2012.
- 426 Chen, M. Y., Xie, P. P., Janowiak, J. E., and Arkin, P. A.: Global land precipitation: A 50-yr monthly analysis based  
427 on gauge observations, *J Hydrometeorol*, 3, 249-266, 10.1175/1525-7541(2002)003<0249:glpaym>2.0.co;2, 2002.
- 428 Chen, Y. N., Zhu, Z. W., Luo, L., and Zhang, J. W.: Severe haze in Hangzhou in winter 2013/14 and associated  
429 meteorological anomalies, *Dyn Atmos Oceans*, 81, 73-83, 10.1016/j.dynatmoce.2018.01.002, 2018.
- 430 Chen, Y. Y., Ebenstein, A., Greenstone, M., and Li, H. B.: Evidence on the impact of sustained exposure to air  
431 pollution on life expectancy from China's Huai River policy, *Proc Natl Acad Sci*, 110, 12936-12941,  
432 10.1073/pnas.1300018110, 2013.
- 433 Chen, Z. Y., Xie, X. M., Cai, J., Chen, D. L., Gao, B. B., He, B., Cheng, N. L., and Xu, B.: Understanding  
434 meteorological influences on PM<sub>2.5</sub> concentrations across China: a temporal and spatial perspective, *Atmos*  
435 *Chem Phys*, 18, 5343-5358, 10.5194/acp-18-5343-2018, 2018.
- 436 Chung, C. E., Ramanathan, V., and Kiehl, J. T.: Effects of the South Asian absorbing haze on the Northeast  
437 monsoon and surface-air heat exchange, *J Climate*, 15, 2462-2476,  
438 10.1175/1520-0442(2002)015<2462:eotsaa>2.0.co;2, 2002.
- 439 CMA: China ground observation data sets, available at: <http://data.cma.cn/>, last access: 10 January 2018 (in  
440 Chinese).
- 441 Dee, D. P., Uppala, S. M., Simmons, A. J., Berrisford, P., Poli, P., Kobayashi, S., Andrae, U., Balmaseda, M. A.,  
442 Balsamo, G., Bauer, P., Bechtold, P., Beljaars, A. C. M., van de Berg, L., Bidlot, J., Bormann, N., Delsol, C.,  
443 Dragani, R., Fuentes, M., Geer, A. J., Haimberger, L., Healy, S. B., Hersbach, H., Hólm, E. V., Isaksen, L.,  
444 Kållberg, P., Köhler, M., Matricardi, M., McNally, A. P., Monge-Sanz, B. M., Morcrette, J. J., Park, B. K.,  
445 Peubey, C., de Rosnay, P., Tavolato, C., Thépaut, J. N., and Vitart, F.: The ERA-Interim reanalysis: configuration  
446 and performance of the data assimilation system, *Q J R Meteorol Soc*, 137, 553-597, 10.1002/qj.828, 2011.
- 447 Ding, Y. H., and Liu, Y. J.: Analysis of long-term variations of fog and haze in China in recent 50 years and their  
448 relations with atmospheric humidity, *Sci China Earth Sci*, 57, 36-46, 10.1007/s11430-013-4792-1, 2014.



- 449 Ding, Y. H., Wu, P., Liu, Y. J., and Song, Y. F.: Environmental and dynamic conditions for the occurrence of  
450 persistent haze events in North China, *Engineering*, 3, 266-271, 10.1016/J.ENG.2017.01.009, 2017.
- 451 ERA-Interim: PBLH data sets, available at: <http://www.ecmwf.int/en/research/climate-reanalysis/era-interim>, last  
452 access: 10 January 2018.
- 453 Gao, H., and Li, X.: Influences of El Nino Southern Oscillation events on haze frequency in eastern China during  
454 boreal winters, *Int J Climatol*, 35, 2682-2688, 10.1002/joc.4133, 2015.
- 455 Gao, Y., and Chen, D.: A dark October in Beijing 2016, *Atmos Oceanic Sci Lett*, 10, 206-213,  
456 10.1080/16742834.2017.1293473, 2017.
- 457 Guo, J. P., Zhang, X. Y., Wu, Y. R., Zhaxi, Y. Z., Che, H. Z., La, B., Wang, W., and Li, X. W.: Spatio-temporal  
458 variation trends of satellite-based aerosol optical depth in China during 1980–2008, *Atmos Environ*, 45,  
459 6802-6811, 10.1016/j.atmosenv.2011.03.068, 2011.
- 460 Guo, S., Hu, M., Zamora, M. L., Peng, J. F., Shang, D. J., Zheng, J., Du, Z. F., Wu, Z. J., Shao, M., Zeng, L. M.,  
461 Molina, M. J., and Zhang, R. Y.: Elucidating severe urban haze formation in China, *Proc Natl Acad Sci*, 111,  
462 17373-17378, 10.1073/pnas.1419604111, 2014.
- 463 He, J. H., and Zhu, Z. W.: The relation of South China Sea monsoon onset with the subsequent rainfall over the  
464 subtropical East Asia, *Int J Climatol*, 35, 4547-4556, 10.1002/joc.4305, 2015.
- 465 Held, I. M., and Suarez, M. J.: A proposal for the intercomparison of the dynamical cores of atmospheric general  
466 circulation models, *Bull Amer Meteor Soc*, 75, 1825-1830, 10.1175/1520-0477(1994)075<1825:apftio>2.0.co;2,  
467 1994.
- 468 Huang, B. Y., Thorne, P. W., Banzon, V. F., Boyer, T., Chepurin, G., Lawrimore, J. H., Menne, M. J., Smith, T. M.,  
469 Vose, R. S., and Zhang, H. M.: Extended Reconstructed Sea Surface Temperature, version 5 (ERSSTv5):  
470 Upgrades, validations, and intercomparisons, *J Climate*, 30, 8179-8205, 10.1175/jcli-d-16-0836.1, 2017.
- 471 Jacob, D. J., and Winner, D. A.: Effect of Climate Change on Air Quality, *Atmos Environ*, 43, 51-63,  
472 10.1016/j.atmosenv.2008.09.051, 2009.
- 473 Jia, B., Wang, Y., Yao, Y., and Xie, Y.: A new indicator on the impact of large-scale circulation on wintertime  
474 particulate matter pollution over China, *Atmos Chem Phys*, 15, 11919-11929, 10.5194/acp-15-11919-2015,  
475 2015.
- 476 Kalnay, E., Kanamitsu, M., Kistler, R., Collins, W., Deaven, D., Gandin, L., Iredell, M., Saha, S., White, G.,  
477 Woollen, J., Zhu, Y., Leetmaa, A., Reynolds, R., Chelliah, M., Ebisuzaki, W., Higgins, W., Janowiak, J., Mo, K.  
478 C., Ropelewski, C., Wang, J., Jenne, R., and Joseph, D.: The NCEP/NCAR 40-year reanalysis project, *Bull*  
479 *Amer Meteor Soc*, 77, 437-471, 10.1175/1520-0477(1996)077<0437:tnyrp>2.0.co;2, 1996.
- 480 Lau, K. M., and Kim, K. M.: Observational relationships between aerosol and Asian monsoon rainfall, and  
481 circulation, *Geophys Res Lett*, 33, L21810, 10.1029/2006GL027546, 2006.
- 482 Lau, K. M., Kim, M. K., and Kim, K. M.: Asian summer monsoon anomalies induced by aerosol direct forcing: the  
483 role of the Tibetan Plateau, *Clim Dyn*, 26, 855-864, 10.1007/s00382-006-0114-z, 2006.
- 484 Li, C., Martin, R. V., Boys, B. L., van Donkelaar, A., and Ruzzante, S.: Evaluation and application of multi-decadal  
485 visibility data for trend analysis of atmospheric haze, *Atmos Chem Phys*, 16, 2435-2457,  
486 10.5194/acp-16-2435-2016, 2016.
- 487 Li, Q., Zhang, R. H., and Wang, Y.: Interannual variation of the wintertime fog–haze days across central and



- 488 eastern China and its relation with East Asian winter monsoon, *Int J Climatol*, 36, 346-354, 10.1002/joc.4350,  
489 2016.
- 490 Li, R., Hu, Y. J., Li, L., Fu, H. B., and Chen, J. M.: Real-time aerosol optical properties, morphology and mixing  
491 states under clear, haze and fog episodes in the summer of urban Beijing, *Atmos Chem Phys*, 17, 5079-5093,  
492 10.5194/acp-17-5079-2017, 2017.
- 493 Li, Z. Q., Lau, W. K. M., Ramanathan, V., Wu, G., Ding, Y., Manoj, M. G., Liu, J., Qian, Y., Li, J., Zhou, T., Fan, J.,  
494 Rosenfeld, D., Ming, Y., Wang, Y., Huang, J., Wang, B., Xu, X., Lee, S. S., Cribb, M., Zhang, F., Yang, X., Zhao,  
495 C., Takemura, T., Wang, K., Xia, X., Yin, Y., Zhang, H., Guo, J., Zhai, P. M., Sugimoto, N., Babu, S. S., and  
496 Brasseur, G. P.: Aerosol and monsoon climate interactions over Asia, *Rev Geophys*, 54, 866-929,  
497 10.1002/2015RG000500, 2016.
- 498 Liu, Y., Sun, J. R., and Yang, B.: The effects of black carbon and sulphate aerosols in China regions on East Asia  
499 monsoons, *Tellus B*, 61, 642-656, 10.1111/j.1600-0889.2009.00427.x, 2009.
- 500 Luan, T., Guo, X. L., Guo, L. J., and Zhang, T. H.: Quantifying the relationship between PM<sub>2.5</sub> concentration,  
501 visibility and planetary boundary layer height for long-lasting haze and fog-haze mixed events in Beijing,  
502 *Atmos Chem Phys*, 18, 203-225, 10.5194/acp-18-203-2018, 2018.
- 503 Mu, M., and Zhang, R. H.: Addressing the issue of fog and haze: A promising perspective from meteorological  
504 science and technology, *Sci China Earth Sci*, 57, 1-2, 10.1007/s11430-013-4791-2, 2014.
- 505 Mu, Q., and Liao, H.: Simulation of the interannual variations of aerosols in China: role of variations in  
506 meteorological parameters, *Atmos Chem Phys*, 14, 9597-9612, 10.5194/acp-14-9597-2014, 2014.
- 507 NCEP/NCAR: NCEP/NCAR Reanalysis data sets, available at: <http://www.esrl.noaa.gov/psd/data>  
508 /gridded/data.ncep.reanalysis.html, last access: 10 January 2018.
- 509 Niu, F., Li, Z. Q., Li, C., Lee, K. H., and Wang, M. Y.: Increase of wintertime fog in China: Potential impacts of  
510 weakening of the Eastern Asian monsoon circulation and increasing aerosol loading, *J Geophys Res*, 115,  
511 D00K20, 10.1029/2009JD013484, 2010.
- 512 NOAA: NOAA Extended Reconstructed Sea Surface Temperature (SST) V5 data sets, available at:  
513 <https://www.esrl.noaa.gov/psd/data/gridded/data.noaa.ersst.v5.html>, last access: 10 January 2018.
- 514 NOAA: NOAA precipitation datasets, available at: <https://www.esrl.noaa.gov/psd/data/gridded/data.prec.html>,  
515 last access: 10 January 2018.
- 516 Pei, L., Yan, Z. W., Sun, Z. B., Miao, S. G., and Yao, Y.: Increasing persistent haze in Beijing: potential impacts of  
517 weakening East Asian winter monsoons associated with northwestern Pacific sea surface temperature trends,  
518 *Atmos Chem Phys*, 18, 3173-3183, 10.5194/acp-18-3173-2018, 2018.
- 519 Pope III, C. A., and Dockery, D. W.: Health effects of fine particulate air pollution: Lines that connect, *J Air Waste*  
520 *Manage*, 56, 709-742, 10.1080/10473289.2006.10464485, 2006.
- 521 Seo, J., Kim, J. Y., Youn, D., Lee, J. Y., Kim, H., Lim, Y. B., Kim, Y., and Jin, H. C.: On the multiday haze in the  
522 Asian continental outflow: the important role of synoptic conditions combined with regional and local sources,  
523 *Atmos Chem Phys*, 17, 9311-9332, 10.5194/acp-17-9311-2017, 2017.
- 524 Takaya, K., and Nakamura, H.: A formulation of a phase-independent wave-activity flux for stationary and  
525 migratory quasigeostrophic eddies on a zonally varying basic flow, *J Atmos Sci*, 58, 608-627,  
526 10.1175/1520-0469(2001)058<0608:afopi>2.0.co;2, 2001.



- 527 Tao, M. H., Chen, L. F., Xiong, X. Z., Zhang, M. G., Ma, P. F., Tao, J. H., and Wang, Z. F.: Formation process of  
528 the widespread extreme haze pollution over northern China in January 2013: Implications for regional air  
529 quality and climate, *Atmos Environ*, 98, 417-425, [10.1016/j.atmosenv.2014.09.026](https://doi.org/10.1016/j.atmosenv.2014.09.026), 2014.
- 530 Tao, M. H., Chen, L. F., Wang, Z. F., Wang, J., Tao, J. H., and Wang, X. H.: Did the widespread haze pollution over  
531 China increase during the last decade? A satellite view from space, *Environ Res Lett*, 11, 054019,  
532 [10.1088/1748-9326/11/5/054019](https://doi.org/10.1088/1748-9326/11/5/054019), 2016.
- 533 Tett, S. F. B., Stott, P. A., Allen, M. R., Ingram, W. J., and Mitchell, J. F. B.: Causes of twentieth-century  
534 temperature change near the Earth's surface, *Nature*, 399, 569-572, [10.1038/21164](https://doi.org/10.1038/21164), 1999
- 535 Tie, X. X., Wu, D., and Brasseur, G.: Lung cancer mortality and exposure to atmospheric aerosol particles  
536 in Guangzhou, China, *Atmos Environ*, 43, 2375-2377, [10.1016/j.atmosenv.2009.01.036](https://doi.org/10.1016/j.atmosenv.2009.01.036), 2009.
- 537 Wang, H. J., Chen, H. P., and Liu, J. P.: Arctic sea ice decline intensified haze pollution in eastern China, *Atmos  
538 Oceanic Sci Lett*, 8, 1-9, [10.3878/AOSL20140081](https://doi.org/10.3878/AOSL20140081), 2015.
- 539 Wang, H. J., and Chen, H. P.: Understanding the recent trend of haze pollution in eastern China: roles of climate  
540 change, *Atmos Chem Phys*, 16, 4205-4211, [10.5194/acp-16-4205-2016](https://doi.org/10.5194/acp-16-4205-2016), 2016.
- 541 Wang, H. J.: On assessing haze attribution and control measures in China, *Atmos Oceanic Sci Lett*, 11, 120-122,  
542 [10.1080/16742834.2018.1409067](https://doi.org/10.1080/16742834.2018.1409067), 2018.
- 543 Wang, J., He, J. H., Liu, X. F., and Wu, B. G.: Interannual variability of the Meiyu onset over Yangtze-Huaihe  
544 River Valley and analyses of its previous strong influence signal, *Chin Sci Bull*, 54, 687-695,  
545 [10.1007/s11434-008-0534-8](https://doi.org/10.1007/s11434-008-0534-8), 2009.
- 546 Wang, J., Zhang, X. Y., Cai, Z. Y., Wang, D. Z., and Chen, H.: Meteorological causes of a heavy air pollution  
547 process in Tianjin and its prediction analyses, *Environ Sci Technol*, 38, 77-82, 2015 (in Chinese).
- 548 Wang, J., Zhao, Q. H., Zhu, Z. W., Qi, L., Wang, J. X. L., and He, J. H.: Interannual variation in the number and  
549 severity of autumnal haze days in the Beijing-Tianjin-Hebei region and associated atmospheric circulation  
550 anomalies, *Dyn Atmos Oceans*, 84, 1-9, [10.1016/j.dynatmoce.2018.08.001](https://doi.org/10.1016/j.dynatmoce.2018.08.001), 2018.
- 551 Wang, Y. S., Yao, L., Wang, L. L., Liu, Z. R., Ji, D. S., Tang, G. Q., Zhang, J. K., Sun, Y., Hu, B., and Xin, J. Y.:  
552 Mechanism for the formation of the January 2013 heavy haze pollution episode over central and eastern China,  
553 *Sci China Earth Sci*, 57, 14-25, [10.1007/s11430-013-4773-4](https://doi.org/10.1007/s11430-013-4773-4), 2014.
- 554 Wang, Z. F., Li, J., Wang, Z., Yang, W. Y., Tang, X., Ge, B. Z., Yan, P. Z., Zhu, L. L., Chen, X. S., Chen, H. S.,  
555 Wang, W., Li, J. J., Liu, B., Wang, X. Y., Wang, W., Zhao, Y. L., Lu, N., and Su, D. B.: Modeling study of  
556 regional severe hazes over mid-eastern China in January 2013 and its implications on pollution prevention and  
557 control, *Sci China Earth Sci*, 57, 3-13, [10.1007/s11430-013-4793-0](https://doi.org/10.1007/s11430-013-4793-0), 2014.
- 558 Wu, D., Tie, X. X., Li, C. C., Ying, Z. M., Kai-Hon Lau, A., Huang, J., Deng, X. J., and Bi, X. Y.: An extremely  
559 low visibility event over the Guangzhou region: A case study, *Atmos Environ*, 39, 6568-6577,  
560 [10.1016/j.atmosenv.2005.07.061](https://doi.org/10.1016/j.atmosenv.2005.07.061), 2005.
- 561 Wu, G. X., Li, Z. Q., Fu, C. B., Zhang, X. Y., Zhang, R. Y., Zhang, R. H., Zhou, T. J., Li, J. P., Li, J. D., Zhou, D.  
562 G., Wu, L., Zhou, L. T., He, B., and Huang, R. H.: Advances in studying interactions between aerosols and  
563 monsoon in China, *Sci China Earth Sci*, 59, 1-16, [10.1007/s11430-015-5198-z](https://doi.org/10.1007/s11430-015-5198-z), 2016.
- 564 Xiao, D., Li, Y., Fan, S. J., Zhang, R. H., Sun, J. R., and Wang, Y.: Plausible influence of Atlantic Ocean SST  
565 anomalies on winter haze in China, *Theor Appl Climatol*, 122, 249-257, [10.1007/s00704-014-1297-6](https://doi.org/10.1007/s00704-014-1297-6), 2015.



- 566 Xu, P., Chen, Y. F., and Ye, X. J.: Haze, air pollution, and health in China, *Lancet*, 382, 2067,  
567 10.1016/S0140-6736(13)62693-8, 2013.
- 568 Xu, X., Zhao, T., Liu, F., Gong, S. L., Kristovich, D., Lu, C., Guo, Y., Cheng, X., Wang, Y., and Ding, G.: Climate  
569 modulation of the Tibetan Plateau on haze in China, *Atmos Chem Phys*, 16, 1365-1375,  
570 10.5194/acp-16-1365-2016, 2016.
- 571 Xu, X. D., Wang, Y. J., Zhao, T. L., Cheng, X. H., Meng, Y. Y., and Ding, G. A.: “Harbor” effect of large  
572 topography on haze distribution in eastern China and its climate modulation on decadal variations in haze China ,  
573 *Chin Sci Bull*, 60, 1132-1143, 10.1360/N972014-00101, 2015 (in Chinese).
- 574 Yang, Y., Liao, H., and Lou, S. J.: Decadal trend and interannual variation of outflow of aerosols from East Asia:  
575 Roles of variations in meteorological parameters and emissions, *Atmos Environ*, 100, 141-153,  
576 10.1016/j.atmosenv.2014.11.004, 2015.
- 577 Yang, Y., Liao, H., and Lou, S. J.: Increase in winter haze over eastern China in recent decades: Roles of variations  
578 in meteorological parameters and anthropogenic emissions, *J Geophys Res Atmos*, 121, 13,050-013,065,  
579 10.1002/2016JD025136, 2016.
- 580 Yang, Y. R., Liu, X. G., Qu, Y., An, J. L., Jiang, R., Zhang, Y. H., Sun, Y. L., Wu, Z. J., Zhang, F., Xu, W. Q., and  
581 Ma, Q. X.: Characteristics and formation mechanism of continuous hazes in China: a case study during the  
582 autumn of 2014 in the North China Plain, *Atmos Chem Phys*, 15, 8165-8178, 10.5194/acp-15-8165-2015, 2015.
- 583 Yin, Z. C., Wang, H. J., and Guo, W. L.: Climatic change features of fog and haze in winter over North China and  
584 Huang-Huai Area, *Sci China Earth Sci*, 58, 1370-1376, 10.1007/s11430-015-5089-3, 2015.
- 585 Yin, Z. C., and Wang, H. J.: The relationship between the subtropical Western Pacific SST and haze over  
586 North-Central North China Plain, *Int J Climatol*, 36, 3479-3491, 10.1002/joc.4570, 2016a.
- 587 Yin, Z. C., and Wang, H. J.: Seasonal prediction of winter haze days in the north central North China Plain, *Atmos  
588 Chem Phys*, 16, 14843-14852, 10.5194/acp-16-14843-2016, 2016b.
- 589 Yin, Z. C., and Wang, H. J.: Role of atmospheric circulations in haze pollution in December 2016, *Atmos Chem  
590 Phys*, 17, 11673-11681, 10.5194/acp-17-11673-2017, 2017.
- 591 Yin, Z. C., Wang, H. J., and Chen, H. P.: Understanding severe winter haze events in the North China Plain in 2014:  
592 roles of climate anomalies, *Atmos Chem Phys*, 17, 1641-1651, 10.5194/acp-17-1641-2017, 2017.
- 593 Yin, Z. C., and Wang, H. J.: The strengthening relationship between Eurasian snow cover and December haze days  
594 in central North China after the mid-1990s, *Atmos Chem Phys*, 18, 4753–4763, 10.5194/acp-18-4753-2018,  
595 2018.
- 596 You, T., Wu, R. G., Huang, G., and Fan, G. Z.: Regional meteorological patterns for heavy pollution events in  
597 Beijing, *J Meteor Res*, 31, 597–611, 10.1007/s13351-017-6143-1, 2017.
- 598 Zhang, H., Zhao, S. Y., Wang, Z. L., Zhang, X. Y., and Song, L. C.: The updated effective radiative forcing of  
599 major anthropogenic aerosols and their effects on global climate at present and in the future, *Int J Climatol*, 36,  
600 4029-4044, 10.1002/joc.4613, 2016.
- 601 Zhang, L., Wang, T., Lv, M. Y., and Zhang, Q.: On the severe haze in Beijing during January 2013: Unraveling the  
602 effects of meteorological anomalies with WRF-Chem, *Atmos Environ*, 104, 11-21,  
603 10.1016/j.atmosenv.2015.01.001, 2015.
- 604 Zhang, R. H., Li, Q., and Zhang, R. N.: Meteorological conditions for the persistent severe fog and haze event over



- 605 eastern China in January 2013, *Sci China Earth Sci*, 57, 26-35, 10.1007/s11430-013-4774-3, 2014.
- 606 Zhang, Z. Y., Zhang, X., Gong, D. Y., Kim, S. J., Mao, R., and Zhao, X.: Possible influence of atmospheric  
607 circulations on winter haze pollution in the Beijing–Tianjin–Hebei region, northern China, *Atmos Chem Phys*,  
608 16, 561-571, 10.5194/acp-16-561-2016, 2016.
- 609 Zhao, S. Y., Zhang, H., and Xie, B.: The effects of El Niño–Southern Oscillation on the winter haze pollution of  
610 China, *Atmos Chem Phys*, 18, 1863–1877, 10.5194/acp-18-1863-2018, 2018.
- 611 Zhu, X. W., Tang, G. Q., Hu, B., Wang, L. L., Xin, J. Y., Zhang, J. K., Liu, Z. R., Munkel, C., and Wang, Y. S.:  
612 Regional pollution and its formation mechanism over North China Plain: A case study with ceilometer  
613 observations and model simulations, *J Geophys Res Atmos*, 121, 14574-14588, 10.1002/2016JD025730, 2016.
- 614 Zhu, Z. W., Li, T., and He, J. H.: Out-of-Phase relationship between boreal spring and summer decadal rainfall  
615 changes in southern China, *J Climate*, 27, 1083-1099, 10.1175/jcli-d-13-00180.1, 2014.
- 616 Zhu, Z. W., and Li, T.: A new paradigm for continental U.S. summer rainfall variability: Asia–North America  
617 teleconnection, *J Climate*, 29, 7313-7327, 10.1175/jcli-d-16-0137.1, 2016.
- 618 Zhu, Z. W., and Li, T.: The record-breaking hot summer in 2015 over Hawaii and its physical causes, *J Climate*, 30,  
619 4253-4266, 10.1175/JCLI-D-16-0438.1, 2017.
- 620 Zhu, Z. W.: Breakdown of the relationship between Australian summer rainfall and ENSO caused by tropical  
621 Indian Ocean SST warming, *J Climate*, 31, 2321-2336, 10.1175/jcli-d-17-0132.1, 2018.
- 622 Zhu, Z. W., and Li, T.: Amplified contiguous United States summer rainfall variability induced by East Asian  
623 monsoon interdecadal change, *Clim Dyn*, 50, 3523-3536, 10.1007/s00382-017-3821-8, 2018.
- 624 Zou, Y. F., Wang, Y. H., Zhang, Y. Z., and Koo, J.-H.: Arctic sea ice, Eurasia snow, and extreme winter haze in  
625 China, *Sci Adv*, 3, e1602751, 10.1126/sciadv.1602751, 2017.
- 626
- 627
- 628
- 629
- 630
- 631
- 632
- 633
- 634
- 635
- 636
- 637
- 638
- 639
- 640
- 641
- 642
- 643
- 644
- 645



## 646 Figures Captions

647 **Figure 1.** Topographic map (shaded; m) for the BTH region and the locations of 20 meteorological sites (colored dots). The dots colored  
 648 red (light red; magenta) represent significant positive temporal correlation coefficients at the 99% (95%; 90%) confidence level between  
 649 the AHD<sub>BTH</sub> and AHD for every individual site on the interannual timescale.

650 **Figure 2.** Time series of the raw AHD<sub>BTH</sub> (black line; days), along with its interdecadal component (blue line; days) and interannual  
 651 component (red line; days), for the period 1960–2017. The gray horizontal line delineates the average climate value of the raw AHD<sub>BTH</sub>  
 652 during 1960–2017.

653 **Figure 3.** The climatological-mean (1960–2017) autumnal (a) Z500 (contours; gpm), UV850 (vectors; m s<sup>-1</sup>) and total cloud (shaded; %),  
 654 and (b) surface relative humidity (shaded; %) and surface air temperature (contours; °C). The gray shaded area denotes the Tibetan  
 655 Plateau, and the blue dashed box delineates the research domain of the BTH region. The letter A represents the center of anticyclonic  
 656 circulation.

657 **Figure 4.** Regressed patterns of autumnal meteorological parameters onto the interannual component of the AHD<sub>BTH</sub>, including (a)  
 658 surface relative humidity (shaded; %), (b) surface air temperature (shaded; °C), (c) surface wind speed (shaded; m s<sup>-1</sup>), (d) SLP (shaded;  
 659 hPa), (e) PBLH (shaded; m), and (f) 500-hPa omega (shaded; 10<sup>-2</sup> Pa s<sup>-1</sup>). Regression coefficients that are significant at the 90%  
 660 confidence level are stippled. The blue dashed box outlines the research domain of the BTH region.

661 **Figure 5.** Regressed anomalies of autumnal (a) 200-hPa geopotential height (Z200; shaded; gpm) and 200-hPa winds (UV200; vectors; m  
 662 s<sup>-1</sup>), (b) Z500 (shaded; gpm) and 500-hPa winds (UV500; vectors; m s<sup>-1</sup>), (c) SST (shaded; °C) and UV850 (vectors; m s<sup>-1</sup>), (d) SLP  
 663 (shaded; hPa) and surface winds (vectors; m s<sup>-1</sup>), and (e) precipitation (shaded; mm day<sup>-1</sup>), with respect to the interannual component of  
 664 the AHD<sub>BTH</sub>. Regression coefficients that are significant at the 95% (90%) confidence level are stippled (cross hatched). In panels (a) and  
 665 (b), only the wind vectors with statistical significance above the 90% confidence level are shown. In panel (c), the two red dashed  
 666 rectangles, labelled R1 and R2, are the key regions where SSTAs are significantly correlated with the interannual component of the  
 667 AHD<sub>BTH</sub>; vectors with scales less than 0.05 m s<sup>-1</sup> are omitted. In panel (d), vectors with scales less than 0.03 m s<sup>-1</sup> are omitted. The blue  
 668 dashed box delineates the research domain of the BTH region. The letters A and C represent the centers of anticyclonic and cyclonic  
 669 anomalies, respectively.

670 **Figure 6.** Time series of the normalized interannual component of the AHD<sub>BTH</sub> (black line), along with the simultaneous SST over R1  
 671 (red line) and R2 (blue line) for the period 1960–2017. The horizontal dashed lines denote 0.8 of the standard deviation. The numerals  
 672 labelled at the bottom represent the correlation coefficients (*r*) between the AHD<sub>BTH</sub> and simultaneous SST over R1 and R2, separately.  
 673 The upper and lower dots in the red line indicate the three highest and lowest years of SST over R1, respectively.

674 **Figure 7.** Regressed anomalies of autumnal UV850 (vectors; m s<sup>-1</sup>) with respect to the simultaneous interannual component of the SST  
 675 over R1. Green arrows represent the wind vectors with statistical significance above the 90% confidence level. The red dashed rectangle  
 676 labelled R1 is the key region where SSTAs are significantly correlated with the interannual component of the AHD<sub>BTH</sub>. The blue dashed  
 677 box delineates the research domain of the BTH region. The gray shaded area denotes the Tibetan Plateau. The letters A and C represent  
 678 the centers of anticyclonic and cyclonic anomalies, respectively.

679 **Figure 8.** The autumnal composite differences of (a) 200-hPa and (b) 500-hPa WAF (vectors; m<sup>2</sup> s<sup>-2</sup>), geopotential height (contours;  
 680 gpm), and relative vorticity (shaded; 10<sup>-5</sup> s<sup>-1</sup>) between the three highest and three lowest years of simultaneous SST over R1 (highest  
 681 minus lowest), as shown in Fig. 6. The red dashed rectangle labelled R1 is the key region where SSTAs are significantly correlated with  
 682 the interannual component of the AHD<sub>BTH</sub>. The blue dashed box delineates the research domain of the BTH region.

683 **Figure 9.** Regressed anomalies of autumnal (a) UV850 (vectors; m s<sup>-1</sup>) and SST (shaded; °C), and (b) precipitation (shaded; mm day<sup>-1</sup>)  
 684 with respect to the simultaneous interannual component of the SST over R2. In panel (a), green arrows represent the wind vectors with  
 685 statistical significance above the 99% confidence level, and vectors with scales less than 0.05 m s<sup>-1</sup> are omitted. Regression coefficients  
 686 that are significant at the 99% confidence level are cross hatched. The dashed red rectangle labelled R2 is the key region where SSTAs  
 687 are significantly correlated with the interannual component of the AHD<sub>BTH</sub>. The blue dashed box delineates the research domain of the BTH  
 688 region. The gray shaded area denotes the Tibetan Plateau. The letter A (C) represents the center of anticyclonic (cyclonic) anomaly.

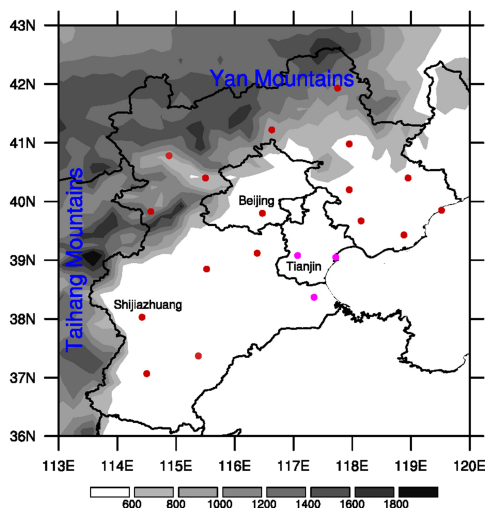
689 **Figure 10.** (a) Latitude–vertical section (112.5°–130°E) of the autumnal omega (shaded; 10<sup>-2</sup> Pa s<sup>-1</sup>) and (b) longitude–vertical section  
 690 (35°–42.5°N) of the autumnal air temperature (shaded; °C) anomalies regressed onto the simultaneous interannual component of the SST  
 691 over R2. Regression coefficients that are significant at the 90% confidence level are stippled. The thick blue horizontal bars superimposed  
 692 onto the abscissa of panels (a) and (b) indicate the latitudes and longitudes of the BTH region, respectively.

693 **Figure 11.** The response of anomalous (a) Z200 (shaded; 10 gpm) and UV200 (vectors; m s<sup>-1</sup>), and (b) Z500 (shaded; 10 gpm) and  
 694 UV500 (vectors; m s<sup>-1</sup>) in H<sub>NAS</sub>. The red contours indicate the imposed idealized heating. The blue dashed box delineates the research  
 695 domain of the BTH region. The letters A and C represent the centers of anticyclonic and cyclonic anomalies, respectively.

696 **Figure 12.** The response of Z850 (shaded; 10 gpm) and UV850 (vectors; m s<sup>-1</sup>) in H<sub>WNP</sub>. The magenta contours indicate the imposed  
 697 idealized heating. The blue dashed box delineates the research domain of the BTH region. The gray shaded area denotes the Tibetan  
 698 Plateau. The letter A (C) represents the center of anticyclonic (cyclonic) anomaly.

699 **Figure 13.** Schematic diagram encapsulating the SSTA-induced (warming in R1 and R2) physical mechanisms and pathways connected to  
 700 above-normal AHD<sub>BTH</sub> years on the interannual timescale. Anomalous quasi-barotropic anticyclones (A) and cyclones (C) are indicated  
 701 by blue and red elliptical cycles with arrows separately, denoting large-scale Rossby wave train triggered by the heating to the north of R1.  
 702 Green arrows depict the key horizontal low-level (850-hPa) airflows. The red, azure and green arrows together exhibit the vertical  
 703 overturning circulation tied to the SST warming in R2. The left-hand (right-hand) side of the cloud-resembled pattern with violet short  
 704 dashed lines presents the significant anomalous precipitation induced by SSTAs over R1 (R2). The blue dashed box delineates the  
 705 research domain of the BTH region.

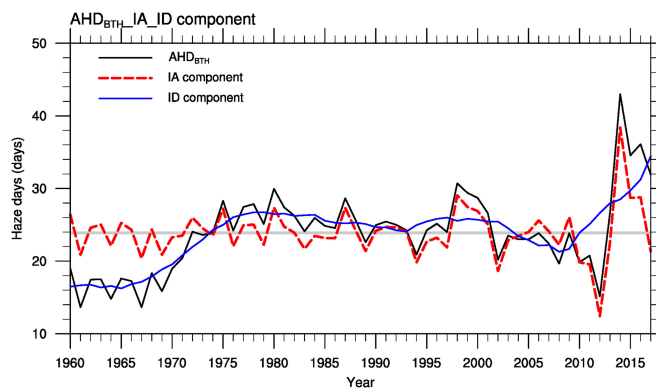
706



707

708 **Figure 1.** Topographic map (shaded; m) for the BTH region and the locations of 20 meteorological sites (colored dots). The dots colored  
709 red (light red; magenta) represent significant positive temporal correlation coefficients at the 99% (95%; 90%) confidence level between  
710 the  $AHD_{BTH}$  and AHD for every individual site on the interannual timescale.

711  
712  
713  
714  
715  
716  
717  
718  
719  
720  
721  
722  
723  
724  
725  
726  
727  
728  
729  
730  
731  
732  
733  
734



735

736 **Figure 2.** Time series of the raw  $AHD_{BTH}$  (black line; days), along with its interdecadal component (blue line; days) and interannual  
737 component (red line; days), for the period 1960–2017. The gray horizontal line delineates the average climate value of the raw  $AHD_{BTH}$   
738 during 1960–2017.

739

740

741

742

743

744

745

746

747

748

749

750

751

752

753

754

755

756

757

758

759

760

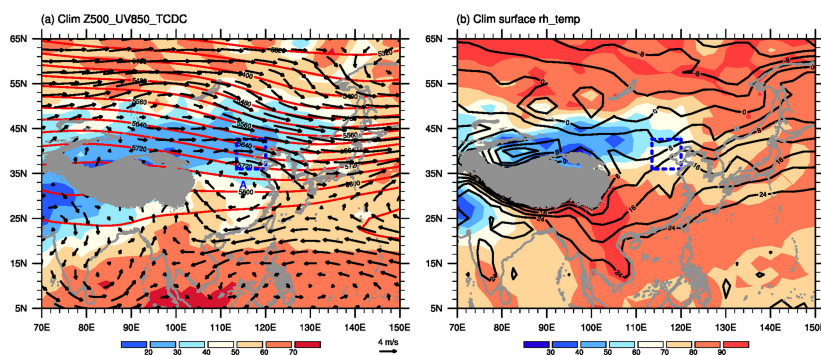
761

762

763

764

765



766

767 **Figure 3.** The climatological-mean (1960–2017) autumnal (a) Z500 (contours; gpm), UV850 (vectors; m s<sup>-1</sup>) and total cloud (shaded; %),  
768 and (b) surface relative humidity (shaded; %) and surface air temperature (contours; °C). The gray shaded area denotes the Tibetan  
769 Plateau, and the blue dashed box delineates the research domain of the BTH region. The letter A represents the center of anticyclonic  
770 circulation.

771

772

773

774

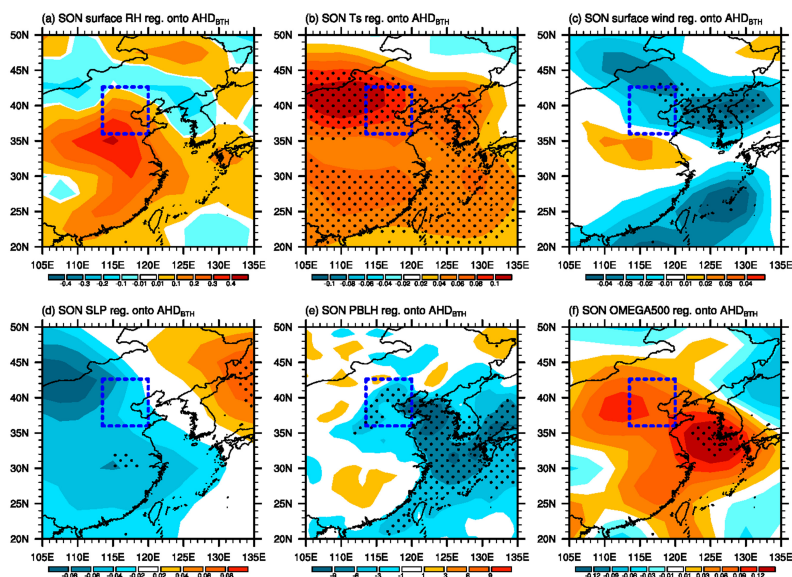
775

776

777

778

779



780

781 **Figure 4.** Regressed patterns of autumnal meteorological parameters onto the interannual component of the  $AHD_{BTH}$ , including (a)  
 782 surface relative humidity (shaded; %), (b) surface air temperature (shaded;  $^{\circ}C$ ), (c) surface wind speed (shaded;  $m s^{-1}$ ), (d) SLP (shaded;  
 783 hPa), (e) PBLH (shaded; m), and (f) 500-hPa omega (shaded;  $10^{-2} Pa s^{-1}$ ). Regression coefficients that are significant at the 90%  
 784 confidence level are stippled. The blue dashed box outlines the research domain of the BTH region.

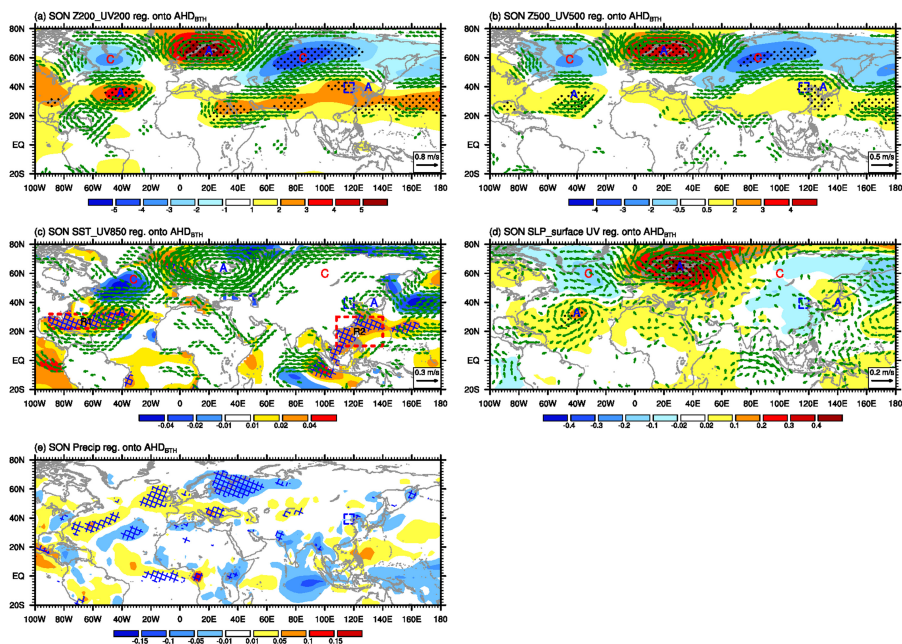
785

786

787

788

789



790

791 **Figure 5.** Regressed anomalies of autumnal (a) 200-hPa geopotential height (Z200; shaded; gpm) and 200-hPa winds (UV200; vectors;  $\text{m s}^{-1}$ ), (b) Z500 (shaded; gpm) and 500-hPa winds (UV500; vectors;  $\text{m s}^{-1}$ ), (c) SST (shaded;  $^{\circ}\text{C}$ ) and UV850 (vectors;  $\text{m s}^{-1}$ ), (d) SLP (shaded; hPa) and surface winds (vectors;  $\text{m s}^{-1}$ ), and (e) precipitation (shaded;  $\text{mm day}^{-1}$ ), with respect to the interannual component of the  $\text{AHD}_{\text{BTH}}$ . Regression coefficients that are significant at the 95% (90%) confidence level are stippled (cross hatched). In panels (a) and (b), only the wind vectors with statistical significance above the 90% confidence level are shown. In panel (c), the two red dashed rectangles, labelled R1 and R2, are the key regions where SSTAs are significantly correlated with the interannual component of the  $\text{AHD}_{\text{BTH}}$ ; vectors with scales less than  $0.05 \text{ m s}^{-1}$  are omitted. In panel (d), vectors with scales less than  $0.03 \text{ m s}^{-1}$  are omitted. The blue dashed box delineates the research domain of the BTH region. The letters A and C represent the centers of anticyclonic and cyclonic anomalies, respectively.

800

801

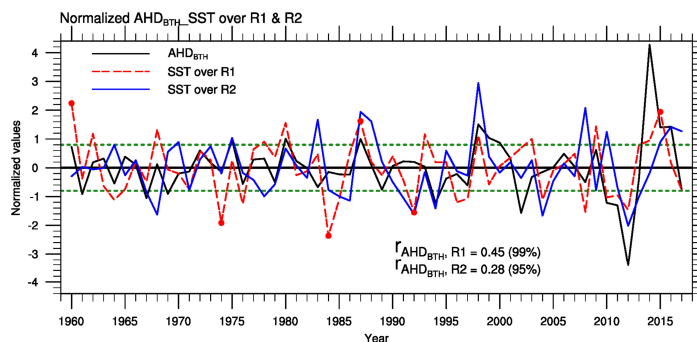
802

803

804

805

806



807

808 **Figure 6.** Time series of the normalized interannual component of the AHD<sub>BTH</sub> (black line), along with the simultaneous SST over R1  
 809 (red line) and R2 (blue line) for the period 1960–2017. The horizontal dashed lines denote 0.8 of the standard deviation. The numerals  
 810 labelled at the bottom represent the correlation coefficients (*r*) between the AHD<sub>BTH</sub> and simultaneous SST over R1 and R2, separately.  
 811 The upper and lower dots in the red line indicate the three highest and lowest years of SST over R1, respectively.

812

813

814

815

816

817

818

819

820

821

822

823

824

825

826

827

828

829

830

831

832

833

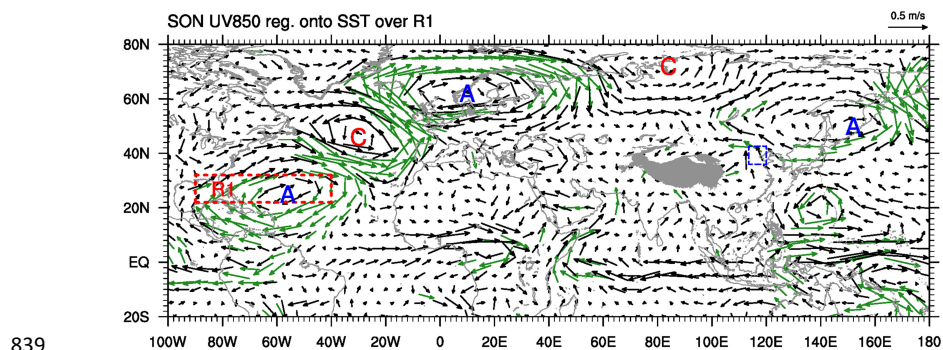
834

835

836

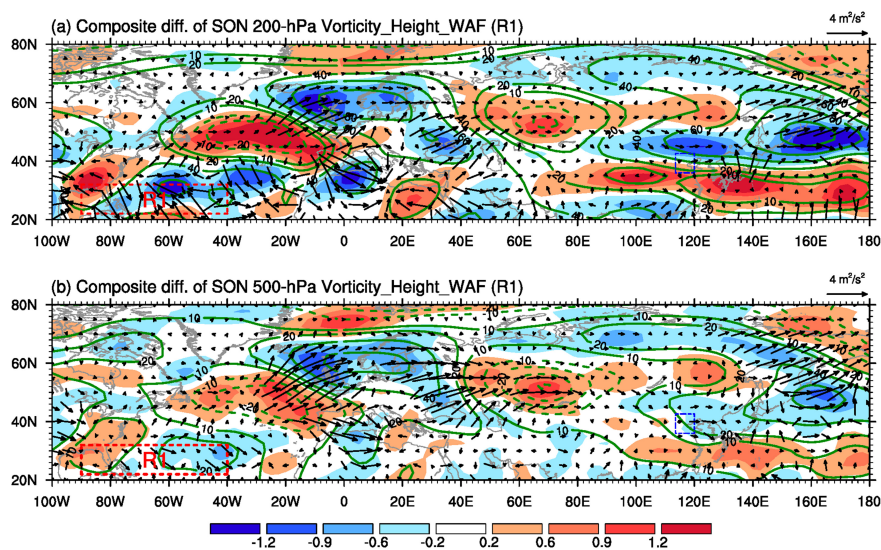
837

838



840 **Figure 7.** Regressed anomalies of autumnal UV850 (vectors;  $\text{m s}^{-1}$ ) with respect to the simultaneous interannual component of the SST  
841 over R1. Green arrows represent the wind vectors with statistical significance above the 90% confidence level. The red dashed rectangle  
842 labelled R1 is the key region where SSTAs are significantly correlated with the interannual component of the  $\text{AHD}_{\text{BTH}}$ . The blue dashed  
843 box delineates the research domain of the BTH region. The gray shaded area denotes the Tibetan Plateau. The letters A and C represent  
844 the centers of anticyclonic and cyclonic anomalies, respectively.

845  
846  
847  
848  
849  
850  
851  
852  
853  
854  
855  
856  
857  
858  
859  
860  
861  
862  
863  
864  
865  
866  
867  
868  
869  
870  
871  
872



873

874 **Figure 8.** The autumnal composite differences of (a) 200-hPa and (b) 500-hPa WAF (vectors;  $\text{m}^2 \text{s}^{-2}$ ), geopotential height (contours;  
875 gpm), and relative vorticity (shaded;  $10^{-5} \text{ s}^{-1}$ ) between the three highest and three lowest years of simultaneous SST over R1 (highest  
876 minus lowest), as shown in Fig. 6. The red dashed rectangle labelled R1 is the key region where SSTAs are significantly correlated with  
877 the interannual component of the  $\text{AHD}_{\text{BTH}}$ . The blue dashed box delineates the research domain of the BTH region.

878

879

880

881

882

883

884

885

886

887

888

889

890

891

892

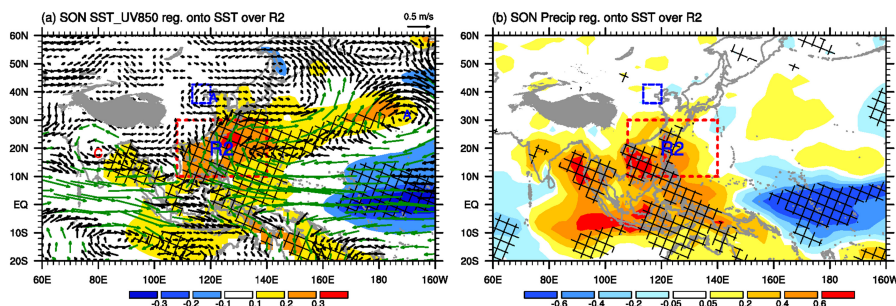
893

894

895

896

897



898

899 **Figure 9.** Regressed anomalies of autumnal (a) UV850 (vectors;  $\text{m s}^{-1}$ ) and SST (shaded;  $^{\circ}\text{C}$ ), and (b) precipitation (shaded;  $\text{mm day}^{-1}$ )  
900 with respect to the simultaneous interannual component of the SST over R2. In panel (a), green arrows represent the wind vectors with  
901 statistical significance above the 99% confidence level, and vectors with scales less than  $0.05 \text{ m s}^{-1}$  are omitted. Regression coefficients  
902 that are significant at the 99% confidence level are cross hatched. The dashed red rectangle labelled R2 is the key region where SSTAs are  
903 significantly correlated with the interannual component of the  $\text{AHD}_{\text{BTH}}$ . The blue dashed box delineates the research domain of the BTH  
904 region. The gray shaded area denotes the Tibetan Plateau. The letter A (C) represents the center of anticyclonic (cyclonic) anomaly.

905

906

907

908

909

910

911

912

913

914

915

916

917

918

919

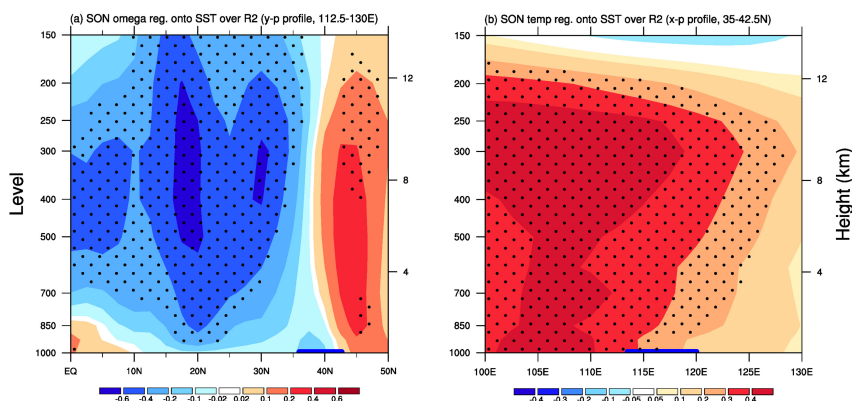
920

921

922

923

924



925

926 **Figure 10.** (a) Latitude–vertical section (112.5°–130°E) of the autumnal omega (shaded;  $10^{-2} \text{Pa s}^{-1}$ ) and (b) longitude–vertical section  
927 (35°–42.5°N) of the autumnal air temperature (shaded; °C) anomalies regressed onto the simultaneous interannual component of the SST  
928 over R2. Regression coefficients that are significant at the 90% confidence level are stippled. The thick blue horizontal bars superimposed  
929 onto the abscissa of panels (a) and (b) indicate the latitudes and longitudes of the BTH region, respectively.

930

931

932

933

934

935

936

937

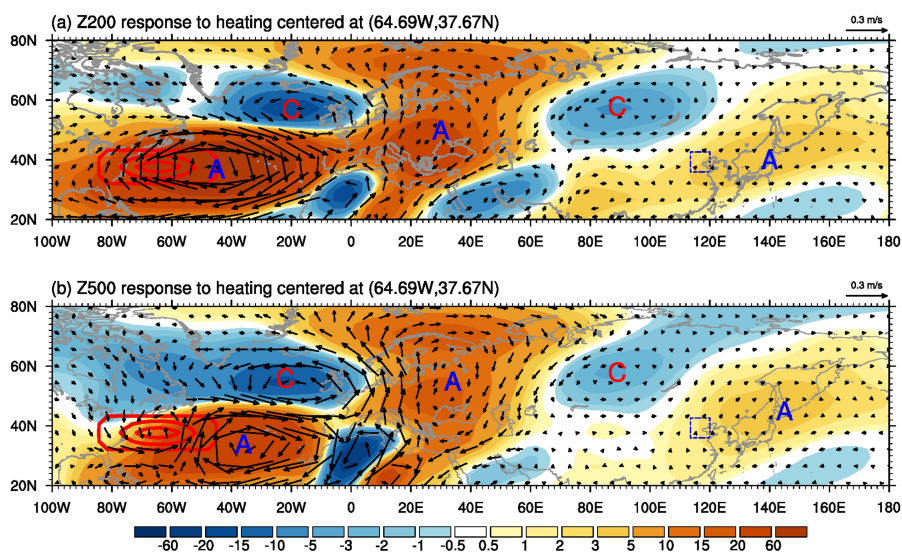
938

939

940

941

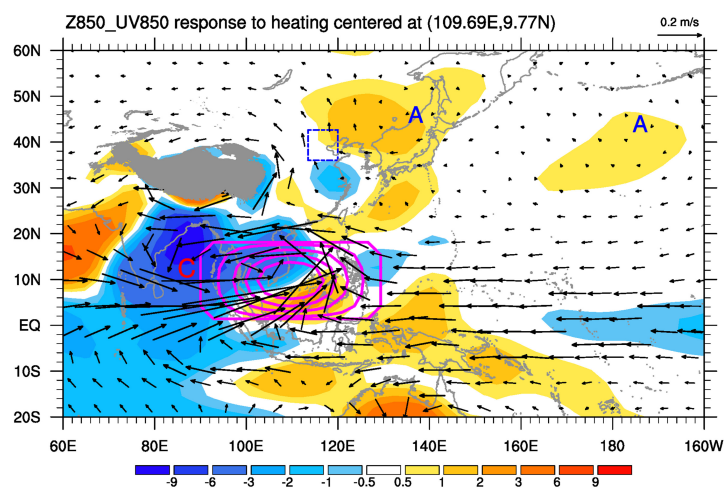
942



943

944 **Figure 11.** The response of anomalous (a) Z200 (shaded; 10 gpm) and UV200 (vectors;  $\text{m s}^{-1}$ ), and (b) Z500 (shaded; 10 gpm) and  
945 UV500 (vectors;  $\text{m s}^{-1}$ ) in H\_NAS. The red contours indicate the imposed idealized heating. The blue dashed box delineates the research  
946 domain of the BTH region. The letters A and C represent the centers of anticyclonic and cyclonic anomalies, respectively.

947  
948  
949  
950  
951  
952  
953  
954  
955  
956  
957  
958  
959  
960  
961  
962  
963  
964  
965  
966  
967  
968  
969  
970  
971



972

973 **Figure 12.** The response of Z850 (shaded; 10 gpm) and UV850 (vectors;  $\text{m s}^{-1}$ ) in H\_WNP. The magenta contours indicate the imposed  
974 idealized heating. The blue dashed box delineates the research domain of the BTH region. The gray shaded area denotes the Tibetan  
975 Plateau. The letter A (C) represents the center of anticyclonic (cyclonic) anomaly.  
976

977

978

979

980

981

982

983

984

985

986

987

988

989

990

991

992

993

994

995

996

997

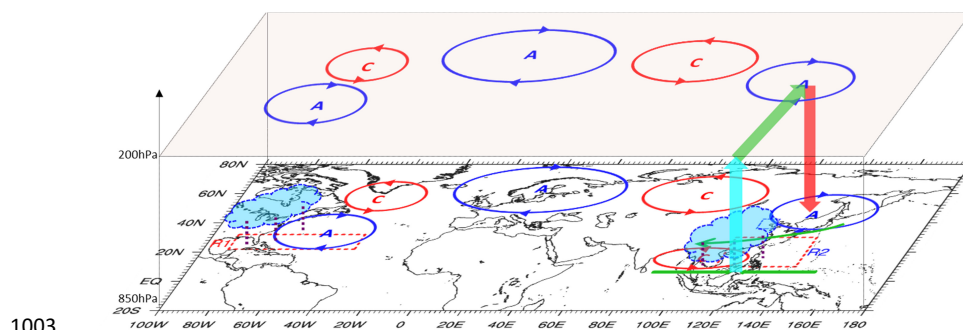
998

999

1000

1001

1002



1003

1004 **Figure 13.** Schematic diagram encapsulating the SSTA-induced (warming in R1 and R2) physical mechanisms and pathways connected  
 1005 to above-normal  $AHD_{BTH}$  years on the interannual timescale. Anomalous quasi-barotropic anticyclones (A) and cyclones (C) are indicated  
 1006 by blue and red elliptical cycles with arrows separately, denoting large-scale Rossby wave train triggered by the heating to the north of R1.  
 1007 Green arrows depict the key horizontal low-level (850-hPa) airflows. The red, azure and green arrows together exhibit the vertical  
 1008 overturning circulation tied to the SST warming in R2. The left-hand (right-hand) side of the cloud-resembling pattern with violet short  
 1009 dashed lines presents the significant anomalous precipitation induced by SSTAs over R1 (R2). The blue dashed box delineates the  
 1010 research domain of the BTH region.

1011

1012

1013

1014

1015

1016

1017

1018

1019

1020

1021

1022

1023

1024

1025

1026

1027

1028

1029

1030

1031

1032

1033

1034

1035

1036

1037

1038

1039